

Contributions of microtubule dynamic instability and rotational diffusion to kinetochore capture

R. Blackwell, O. Sweezy-Schindler, C. Edelmaier, Z. R. Gergely, P. J. Flynn, S. Montes, A. Crapo, A. Doostan, J. R. McIntosh, M. A. Glaser, and M. D. Betterton

Abstract

Microtubule dynamic instability allows search and capture of kinetochores during spindle formation, an important process for accurate chromosome segregation during cell division. Recent work has found that microtubule rotational diffusion about minus-end attachment points contributes to kinetochore capture in fission yeast, but the relative contributions of dynamic instability and rotational diffusion are not well understood. We have developed a biophysical model of kinetochore capture in small fission-yeast nuclei using hybrid Brownian dynamics/kinetic Monte Carlo simulation techniques. With this model, we have studied the importance of dynamic instability and microtubule rotational diffusion for kinetochore capture, both to the lateral surface of a microtubule and at or near its end. Over a range of biologically relevant parameters, microtubule rotational diffusion decreased capture time, but made a relatively small contribution compared to dynamic instability. At most, rotational diffusion reduced capture time by 25%. Our results suggest that while microtubule rotational diffusion can speed up kinetochore capture, it is unlikely to be the dominant physical mechanism for typical conditions in fission yeast. In addition, we found that when microtubules undergo dynamic instability, lateral captures predominate even in the absence of rotational diffusion. Counterintuitively, adding rotational diffusion to a dynamic microtubule increases the probability of end-on capture.

Key words: mitosis; cytoskeleton; microtubules; kinetochores; kinetochore capture

Introduction

Cell division is essential to the propagation of life. For a cell to divide successfully, each daughter cell must inherit the correct genetic material. In eukaryotes, segregation of duplicated chromosomes is performed by the mitotic spindle, a cellular machine composed of microtubules (MTs) and their associated proteins (1). Specialized sites on the chromosomes called kinetochores (KCs) attach to spindle MTs, and these KC-MT attachments are necessary for proper chromosome segregation. Understanding KC capture by spindle MTs and the subsequent chromosome movements is challenging because the process depends on multiple overlapping mechanisms (2–4), including the action of multiple KC-associated motors and highly dynamic MTs that maintain KC attachment during significant MT turnover. Numerous proteins localize to MT plus ends and KCs, but the roles of these different proteins are not yet clear (5–7). Problems in kinetochore-MT attachment and chromosome segregation can lead to aneuploidy, which is associated with birth defects and cancer progression (8).

The discovery of MT dynamic instability 30 years ago (9) led to the proposal that MT search and capture is the primary mechanism of initial KC-MT attachment in mitosis. In this picture, dynamic MTs grow in different directions from centrosomes and make end-on attachments with KCs (10–13). Perturbations to MT dynamics are predicted to have significant effects on KC capture (12), suggesting that dynamic instability is a key component of any KC capture model. Search and capture has been directly observed in large cells (14). However, the simplest search-and-capture mechanism does not appear rapid enough to capture multiple chromosomes quickly enough to match measured time in mitosis. Extensions to the search-and-capture mechanism that can make KC capture more rapid in large cells or cell extracts include KC diffusion (12, 15), MT growth that is spatially biased toward chromosomes (16–18), chromosome spatial arrangements and rotation (15, 19, 20) and KC-initiated MTs that can interact with searching MTs (15, 21, 22). KCs in human cells change size and shape during mitosis, which can both speed up capture and minimize errors (20).

KC capture may occur differently in smaller cells. Lateral KC contacts have been directly observed both in budding yeast (23) and fission yeast (24). Recent work on the small cells of fission yeast found that lateral KC attachment to MTs that rotationally diffuse about their attachment points at the spindle-pole bodies (SPBs, the yeast centrosomes) enabled rapid KC capture, even for relatively less dynamic MTs (24). Here we use the term rotational diffusion for diffusive movements about MT minus-end attachment points, termed pivoting in previous work. Based on experiments and a biophysical model, this work concluded that MT rotational diffusion was the primary determinant of the time to capture lost KCs in these cells. This important finding suggests that MT rotational diffusion may significantly contribute to efficient KC capture, an effect that has been neglected previously. Since initial KC captures are typically lateral rather than end-on (14, 19, 20, 23–25), MT rotational diffusion about minus-end attachment points could be an important determinant of the capture time.

We have sought to evaluate the relative importance of MT dynamic instability versus MT rotational diffusion to KC capture. Previous theoretical work has focused either on MT dynamic instability (11, 12, 15, 17, 20, 26) or rotational diffusion (24); as a result, this work has been unable to compare the two mechanisms and determine their relative importance. One model examined the relative contributions of dynamic instability and rotational diffusion for a single parameter set and found that turning off rotational diffusion caused a modest increase in the mean capture time (27). Because MT rotational diffusion can lead to significant increases in the effective volume searched by a single MT, search-and-capture models that neglect MT rotational diffusion could lead to incorrect conclusions.

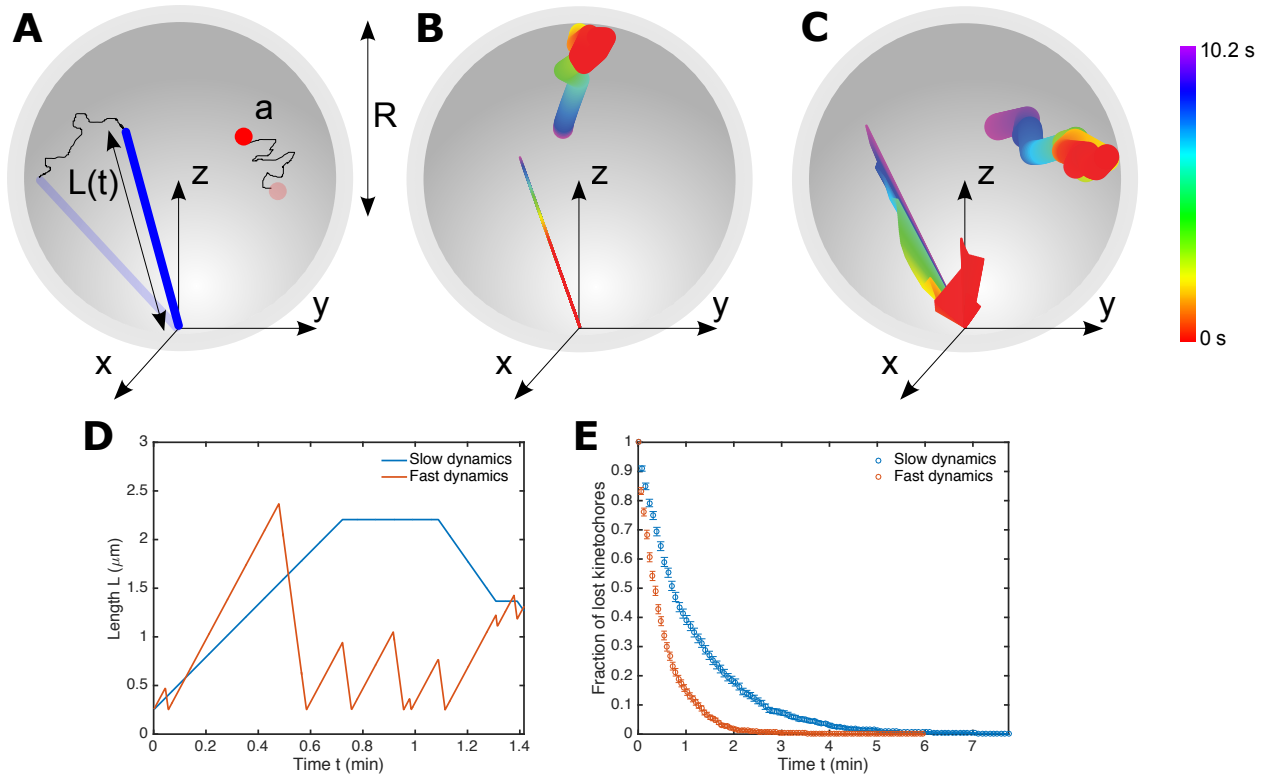


Figure 1: Kinetochore capture model overview. (A) Model schematic. A dynamic microtubule (blue) undergoes dynamic instability and rotational diffusion about its minus-end attachment point; a kinetochore (red) undergoes translational diffusion within the spherical fission-yeast nucleus (gray). (B,C) Images created from simulation data showing microtubule (line) and kinetochore (circle) dynamics. Color indicates time, where red reflects an early position, purple a late one. (B) Model with microtubule dynamic instability but no rotational diffusion. (C) Model with dynamic instability and microtubule rotational diffusion. (D) Microtubule length and (E) fraction of lost kinetochores versus time for slow (blue) and fast (orange) models with the reference parameters (table 1).

We extended the Kalinina *et al.* model of fission-yeast KC capture (24) to include both MT rotational diffusion and dynamic instability in order to gauge their relative importance to KC capture. We modeled both relatively slow dynamic instability (using measured parameters (24)) and faster dynamic instability based on our measurements of single mitotic MTs in fission yeast. Rotational diffusion typically gave only a modest speed-up of KC capture in our model. For slow dynamics, rotational diffusion decreased the KC capture time by up to 25%, while for faster MT dynamics, rotational diffusion caused at most a 16% decrease in the capture time. Our results suggest that the capture time in fission yeast is primarily determined by MT search and capture. We also found that while lateral captures are typical even in the model with no rotational diffusion, including MT diffusion made end-on attachments more likely. This occurred because rotational diffusion sweeps the tip of the MT through space, increasing the volume searched by the tip. Our findings suggest that associating search and capture with end-on attachment and rotational diffusion with lateral attachment is oversimplified.

Materials and methods

Kinetochore capture model

We developed a computational model of KC capture in fission yeast that includes the key physical effects of MT dynamic instability and rotational diffusion. Capture occurs within the spherical nucleus of radius $R = 1.5 \mu\text{m}$. A dynamic MT has its minus end attached to the SPB (which is fixed for this study), rotationally diffuses, and has a length $L(t)$ that changes with time due to dynamic instability (fig. 1, S1). Simultaneously, a spherical KC of radius $a = 100 \text{ nm}$ diffuses in the nucleus (24). We assumed the fission yeast KC size remained constant during mitosis, in contrast to recent work on human KCs (20). KC capture occurs when the KC contacts the MT, either at its end or along its lateral wall.

The simulations used a hybrid Brownian dynamics-kinetic Monte Carlo scheme approach based on our previous work (28–31). Brownian dynamics model the diffusive random motion of MTs and KCs; kinetic Monte Carlo models the stochastic MT dynamic instability (Supporting Material).

Slow and fast microtubule dynamics

We studied two MT dynamic instability models that represent relatively slow and fast dynamics (Supporting Material, fig. 1, table 1). Kalinina *et al.* found that MT dynamics were relatively slow and MTs spent most of their time paused (24). Therefore, we modeled MTs with growing, shrinking, or paused states; the fixed-length paused state is an intermediate between the growing and shrinking states (Supporting Material). In other work on single fission yeast mitotic (32) and meiotic (27) MTs and our measurements, MT dynamics were faster and pausing was rarely seen. We modeled this with growing and shrinking states only, where catastrophe is the transition from growing to shrinking, and rescue the transition from shrinking to growing.

In our model, MTs in the growing or shrinking state increase or decrease in length at the constant speed v_g or v_s . For MTs that are not interacting with the nuclear envelope boundaries, the state switching frequencies are constant in time. Any shrinking MTs that reach the minimum length of $4\sigma_{MT} = 100 \text{ nm}$ switch to the growing state (Supporting Material).

Microtubule interactions with the nuclear envelope

MTs that touch the nuclear envelope experience steric forces and torques from the interaction of the MT tip with the envelope (Supporting Material). The torque can cause the MT tip to slip along the edge of the envelope, reorienting the MT, as has been measured and modeled previously for MTs interacting with microchamber boundaries (33–35). In addition, MTs that grow into a boundary exhibit increased catastrophe frequency (36). The force component along the MT long axis increases the catastrophe frequency, as measured previously (37, 38). By combining these previous measurements of the force dependence of MT growth speed with the growth speed dependence of the catastrophe time, we wrote the catastrophe frequency $f_c(F_{||}) = f_c \exp(\alpha F_{||})$, where $F_{||}$ is the component of the steric force along the MT long axis, α is the force sensitivity of catastrophe (table 1), and f_c is the zero-force catastrophe frequency (or the analogous grow-to-pause frequency in the model with pausing).

Initial conditions and measurements

We began simulations with a single MT of length $4\sigma_{MT}$ (100 nm) placed at a random angle subject to the requirement that the MT was not initially interacting with the nuclear envelope. We inserted

a KC at a random position uniformly sampled within the simulation volume, with the requirement that the KC was not initially interacting with either the MT or the nuclear envelope. We ran the simulation until the KC collided with the MT (either laterally or end-on), which defined a capture. For each parameter set, we repeated simulations 2000-5000 times to determine the distribution of capture times, shown as the fraction of lost KCs as a function of time in figs. 1D, S2. From these data, we computed the mean capture time $\langle \tau_c \rangle$.

We defined reference parameter sets and wide parameter ranges around the reference for both the slow and fast dynamic instability models (table 1). For both slow and fast models, we performed simulations of dynamic instability with no MT rotational diffusion, and dynamic instability plus MT rotational diffusion. To connect to previous search-and-capture models, MTs that shrink to the minimum length re-enter the growing state with a new random orientation.

Experimental methods

To understand the difference between previous measurements of fission-yeast mitotic MT dynamics that were relatively slow (24) or fast (32), we measured MT dynamic instability in *S. pombe*. To facilitate these measurements, we used a strain with temperature-sensitive inactivation of kinesin-5 motors (*cut7-24* in fission yeast) and low-level fluorescent tagging with *mCherry-atb2* (39) (Supporting Material, table S1). Cells carrying the *cut7-ts* allele are unable to form bipolar mitotic spindles at restrictive temperature (36-37°C) (40). The cells instead form monopolar mitotic spindles, in which individual fluorescently labeled mitotic MTs can be imaged (fig. 2) (41).

Measurement of labeled tubulin fraction

We performed immunoblots using the TAT-1 tubulin antibody on *S. pombe* cell lysate with serial dilutions ranging from 100%-10% of the original cell suspension concentration (Supporting Material) and scanned the bands for analysis. The two lower, darker bands corresponded to α -tubulin-1 (*nda2*) at 51 kDa and α -tubulin-2 (*atb2*) at 50 kDa, while the fainter third band corresponded to mCherry-atb2 at 79 kDa (fig. 2). To analyze the scanned images, we inverted the images so that labeled regions corresponded to high intensity, drew equally-sized regions of interest around each band, and determined the average pixel intensity in each region. From this, we determined the fraction of intensity in the mCherry-atb2 band relative to the total. Each lane had similar ratios (data not shown), and we averaged the results for each lane.

Cell preparation and confocal imaging

We grew cells using standard techniques (Supporting Material) and cultured them on glass-bottomed dishes at 36°C for 2-4 hrs to allow monopolar spindles to form. The dishes were transferred to the microscope in less than 60 sec to prevent the monopolar spindles from becoming bipolar. Images were taken on a spinning disk (Yokogawa, Musashino, Japan) Nikon Eclipse Ti inverted confocal microscope (Nikon, Tokyo, Japan) with a 100X, 1.4 NA Plan Apo oil-immersion objective, an iXon Ultra 897 EM-CCD camera (Andor, Belfast, United Kingdom) and a TIZSH Stage Top incubator (Tokai Hit, Fujinomiya, Japan) warmed to 36°C. Three-dimensional images were obtained with an EM Gain of 300, and an exposure time per plane of 40 to 150 msec with 595 nm laser illumination for each of 5 focal planes separated by 500 nm in z, and subsequent stacks are separated by 4-6 sec. Images of fig. 2A are displayed as pixel-interpolated maximum-intensity projections.

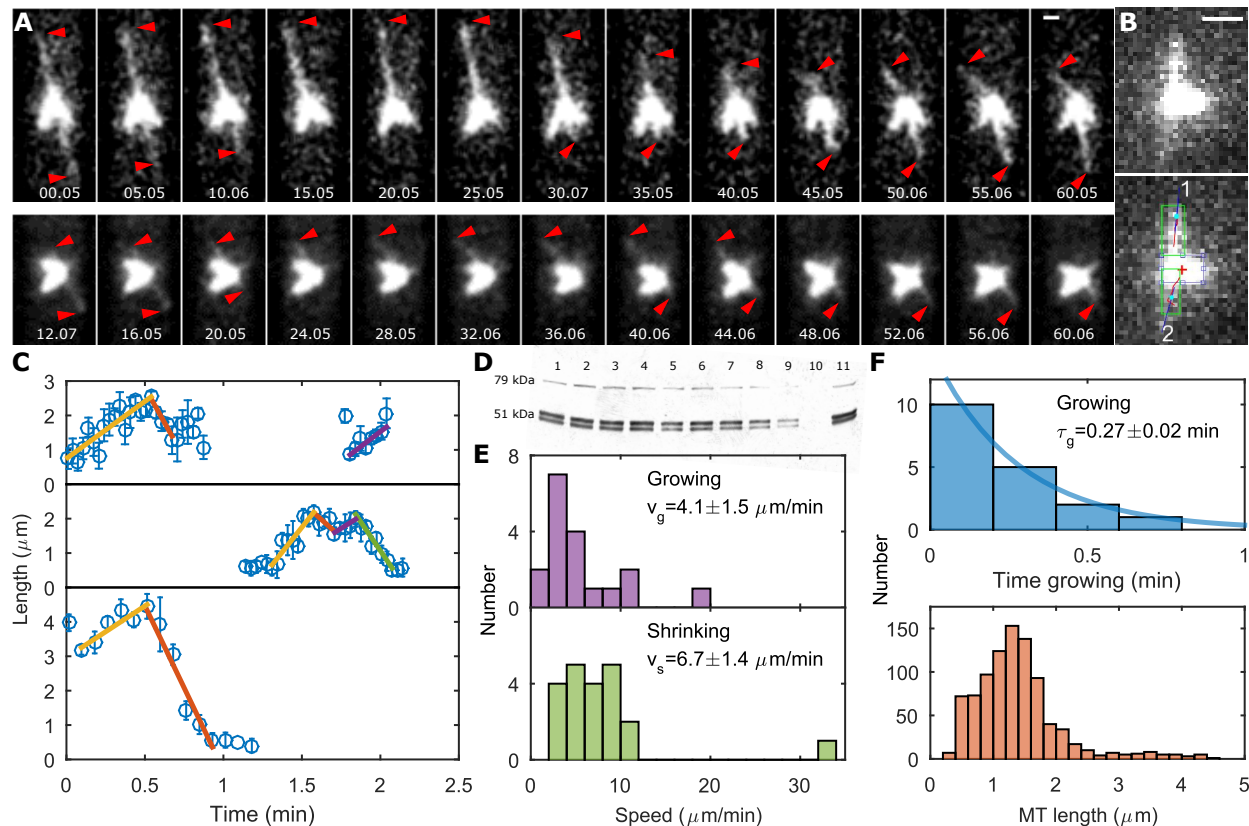


Figure 2: Measurements of single MT dynamics and length in monopolar mitotic spindles. (A) Image sequences. Images are pixel-interpolated maximum intensity projections of monopolar spindles with mCherry-labeled MTs. Red arrowheads indicate single MTs, time is shown in sec, and the scale bar is $1 \mu\text{m}$. (B) Example raw maximum-intensity-projected image (top) and analyzed image (lower). The red cross indicates the center of brightness of the SPB, green boxes the regions analyzed near MT tips, blue lines the fits to the MT backbone positions, and blue dots the fits to the MT tip positions. The scale bar is $1 \mu\text{m}$. (C) Example traces of MT length versus time (points) and fits to growing and shrinking events (lines). (D) Western blot used to quantify fraction of fluorescently labeled tubulin. The gel was loaded with serial dilutions from 100–10% with 100% repeated in lane 11: lane 1=100%, lane 2=90%, lane 3=80%, lane 4=70%, lane 5=60%, lane 6=50%, lane 7=40%, lane 8=30%, lane 9=20%, lane 10=10%, lane 11=100%. (E) Histograms of growth speed and shrinking speed. (F) Histograms of growth time and MT length.

Image and data analysis

In our images of monopolar spindles, we were able to observe dynamic MTs (fig. 2). We quantified the dynamic instability of mitotic MTs by determining the location of the SPBs and the tip of each emanating MT with image analysis software adapted from TipTracker (42, 43). To identify the center of the monopolar spindle, we noted that near the two spindle-pole bodies (SPBs), many short and overlapping MTs produce a bright fluorescent region. When using this software, one selects a rectangle around this region, and our program then computes the center of intensity within that region to estimate the SPB location and determines the length of each MT in a given frame by assuming the MT formed a line between the estimated SPB location and the MT tip position. Visual inspection of each frame confirmed that MTs in the monopolar spindles formed in these cells were typically straight lines emanating from the bright spindle center region (fig. 2B). Each frame is analyzed separately, and the MT length data stored for analysis. The software allows us to make MT length and angle measurements with subpixel resolution and quantify the lengths and dynamics of mitotic MTs in monopolar spindles.

Parameter	Symbol	Reference value	Range	Notes
Nuclear envelope radius	R	1.5 μm	–	Kalinina et al. (24)
KC diameter	σ_{KC}	200 nm	–	Ding et al. (44)
MT diameter	σ_{MT}	25 nm	–	Alberts et al. (45)
MT angular diffusion coefficient	D_θ	–	Varies with MT length	Kalinina et al. (24), Supporting Material
Force-induced catastrophe constant	α	0.5 pN ⁻¹	–	Dogterom and Yurke (37) and Janson et al. (38)
Slow dynamic instability model				
Growth speed	v_g	2.7 $\mu\text{m min}^{-1}$	0.7–11 $\mu\text{m min}^{-1}$	Kalinina et al. (24)
Shrinking speed	v_s	3.8 $\mu\text{m min}^{-1}$	1–16 $\mu\text{m min}^{-1}$	Kalinina et al. (24)
Grow-to-pause frequency	f_{+0}	1.8 min ⁻¹	0.4–7.1 min ⁻¹	Kalinina et al. (24)
Shrink-to-pause frequency	f_{-0}	2.53 min ⁻¹	1.2–5 min ⁻¹	Kalinina et al. (24)
Pause-to-shrink frequency	f_{0-}	0.49 min ⁻¹	0.2–1 min ⁻¹	Kalinina et al. (24)
Pause-to-grow frequency	f_{0+}	0 min ⁻¹	–	Transitions from pausing to growing appeared infrequent in Kalinina et al. (24)
Fast dynamic instability model				
Growth speed	v_g	4.1 $\mu\text{m min}^{-1}$	1–10 $\mu\text{m min}^{-1}$	This work
Shrinking speed	v_s	6.7 $\mu\text{m min}^{-1}$	5–25 $\mu\text{m min}^{-1}$	This work and Sagolla et al. (32)
Catastrophe frequency	f_{cat}	3.7 min ⁻¹	1–8 min ⁻¹	This work
Rescue frequency	f_{res}	0.175 min ⁻¹	0–8 min ⁻¹	This work

Table 1: Model parameter values.

We identified growth and shrinking events by comparing the movies and plots of MT length versus time to identify starting and ending times of events. We then performed weighted least-squares linear fits to the MT length versus time during each event (fig. 2). Growth and shrinking speeds were the slopes determined from the fits, and the catastrophe and rescue times were the duration of the events before a switch.

Results and discussion

Experimental results

Kalinina *et al.* (24) found that fission yeast mitotic MTs on average spent 75% of their time in a paused state and had lifetimes of 3 min, growth speed $v_g = 2.7 \mu\text{m min}^{-1}$, and shrinking speed $v_s = 3.8 \mu\text{m min}^{-1}$. These results differed from the results of Sagolla *et al.* (32), who observed highly dynamic polar MTs in early mitosis (before spindle formation), with lifetimes of seconds and a shrinking speed $v_s = 20 \mu\text{m min}^{-1}$, and more recent work on meiotic MTs (27). These differences in lifetime and dynamics could be related to the stage of mitosis (before and after spindle formation), the number of MTs per bundle, and/or to the fraction of fluorescent tubulin in the cells (which affects MT dynamics (46)). The differences are most likely due to MT bundling, which alters MT dynamics (47, 48). Since KC capture could occur either by single MTs that are more dynamic or bundled MTs that are more stable, we undertook additional measurements of mitotic MT dynamic instability in *S. pombe*.

We adapted the strategy of Costa *et al.* (41), who used temperature-sensitive inactivation of the kinesin-5 motor (*cut7-24*) to obtain cells stably arrested in a monopolar state. Fission yeast carrying the *cut7-ts* allele arrest in early mitosis at restrictive temperature (36–37°C), because

bipolar spindles cannot form when cut7p is inactive (40). These cells instead form monopolar mitotic spindles, in which individual fluorescently labeled mitotic MTs can be imaged and tracked (fig. 2A, B) (41).

To measure MT length, we adapted the TipTracker algorithm (42, 43) to measure MT lengths in monopolar spindles (Methods, fig. 2B). Brighter MTs showed lengths that were more stable in time, and dimmer MTs showed more rapid dynamics (fig. 2A). We identified the dimmer, more dynamic MTs as single MTs, as in previous work (41). We analyzed 20 MTs from 15 cells that showed low intensity compared to other MTs in the same cell and relatively fast dynamics. We determined growth and shrinking events and their associated speeds and times (fig. 2C, Methods).

Fluorescent-protein fusions to tubulin in fission yeast can alter MT dynamics (46). We studied fission yeast carrying *mCherry-atb2* that is an additional copy of this α -tubulin gene under a weak promoter (39). We used Western blotting to determine the fraction of tubulin our cells that was fluorescently tagged (fig. 2D, Methods) and found a low fraction of $8.8\% \pm 0.5\%$ labeled α -tubulin.

These MTs had a median growth speed $v_g = 4.1 \pm 1.5 \mu\text{m min}^{-1}$ and shrinking speed $v_s = 6.7 \pm 1.4 \mu\text{m min}^{-1}$ (fig. 2E). The distribution of times in the growing state appeared exponential with a characteristic time $\tau_g = 0.27 \pm 0.02 \text{ min}$, implying a catastrophe frequency of 3.7 min^{-1} (fig. 2F). Measuring the rescue frequency was challenging, because it was difficult to distinguish rescue from complete shrinkage followed by regrowth of a different MT in the same area. We saw one possible rescue event, which gave a bound $f_r \leq 0.175 \text{ min}^{-1}$.

Our data were collected at 37°C , and MT dynamic instability is sensitive to temperature (49). However, Kalinina *et al.* found relatively little change in fission-yeast MT dynamic instability parameters between 24°C and 32°C (24), suggesting that *S. pombe* mitotic MT dynamic instability may not vary markedly with temperature in this regime. Another possible complication is that MT dynamics might be altered in the monopolar spindle system where kinesin-5 is inactive. Previous work in budding yeast found that kinesin-5s promote disassembly of longer MTs (50). However, since we found similar MT mean lengths to those of Kalinina *et al.* (24), it appears that our measurements do not show a strong bias toward longer MTs due to loss of kinesin-5-associated depolymerization activity.

Pooled length measurements of MTs we identified as single MTs (including all measurements, not just points identified as growing/shrinking events) had a median $\langle L \rangle = 1.31 \pm 0.02 \mu\text{m}$ (fig. 2F). We compared this to the predicted mean length for dynamic instability in an infinite volume (neglecting boundary effects): in the bounded growth regime $\langle L \rangle = v_g v_s / (v_s f_c - v_g f_r)$ (51). If we estimate the mean length using our median dynamic instability parameters with the upper bound on the rescue frequency of $f_r \leq 0.175 \text{ min}^{-1}$, we predict $\langle L \rangle = 1.14 \mu\text{m}$, while using $f_r = 0$ gives $\langle L \rangle = 1.11 \mu\text{m}$. There is little difference between these values, showing that the mean MT length is primarily determined by the growth speed and catastrophe frequency in this low-rescue-frequency regime. This typical MT length estimated from the dynamic instability parameters is consistent with our direct measurements of MT length.

Model results

Kinetochore capture by single microtubules with fast or slow dynamic instability

Since KC capture could occur either by single MTs that are more dynamic or bundled MTs that are more stable, we sought to understand how these different MT arrangements affect KC capture in fission yeast. We studied two reference parameter sets that we denote *slow* (based on the Kalinina *et al.* measurements) and *fast* (based on our measurements). In the slow model, MTs can be growing, shrinking, or paused. The reference parameter values (table 1) were taken from Kalinina

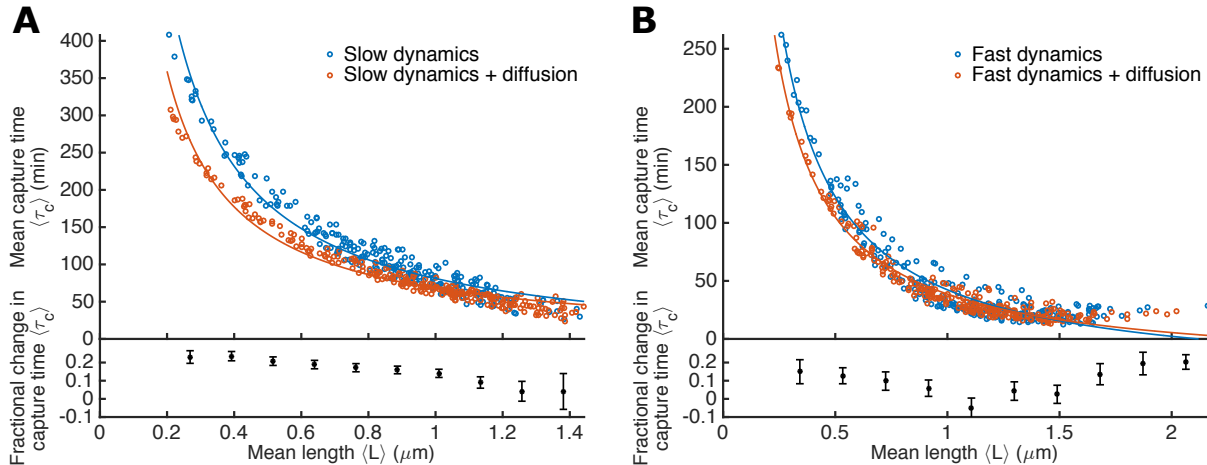


Figure 3: Dependence of capture time on MT length and rotational diffusion. (A) Slow model. (B) Fast model. Points are results simulations with all dynamics parameters varied for search and capture only (blue) and search and capture with microtubule rotational diffusion (orange). Lines are fits to $\langle \tau_c \rangle = A\langle L \rangle^{-1} + B$. Insets, fractional decrease in capture time when rotational diffusion is added to the model. Error bars are determined using standard error propagation techniques from the standard error of the mean capture time in each bin of simulations.

et al., (24) assuming that transitions from pausing to growing did not occur. In the fast model, we considered only growing and shrinking states with reference parameter values determined from our measurements. Examples of the resulting MT length as a function of time and the dynamics of KC capture are shown in figure 1. For each model, we varied parameters around the reference values by factors of 4–20 (table 1) so that we could study the dependence of the capture time on parameter values. We then studied both slow and fast models with and without MT rotational diffusion, to determine the contributions of dynamic instability alone and dynamic instability with rotational diffusion to the capture time.

Kalinina *et al.* found that 3 polar MTs were typically visible during their KC capture experiments, and that the time of KC capture was sensitive to MT number (24). Here we determined capture times for a single MT. Our model results for capture by a single MT and slow dynamic instability agree well with those of Kalinina *et al.* (fig. S2). Studying capture by single MTs allowed us to focus on the effect of dynamic instability parameters and rotational diffusion.

Parametric study using polynomial chaos expansion

To understand how the mean capture time $\langle \tau_c \rangle$ and the mean MT length $\langle L \rangle$ depend on model parameters (table 1), we used polynomial chaos (PC) expansion (52, 53), a widely used technique for uncertainty quantification. PC expansion is a type of spectral method in which we represent $\langle \tau_c \rangle$ and $\langle L \rangle$ as functions of the dynamic instability parameters in a high-order, multivariate, orthogonal polynomial basis, here of Legendre type. This allowed us to use a relatively small number of simulations, corresponding to random samples of input parameters generated uniformly over their allowed ranges (table 1), to accurately approximate $\langle \tau_c \rangle$ and $\langle L \rangle$ over the full multidimensional parameter space (54–56). We then used this expansion to perform global and local sensitivity analysis to determine which dynamic instability parameters are of most importance to $\langle \tau_c \rangle$ and $\langle L \rangle$. The global sensitivity analysis provides information on the importance of each parameter in terms of its contribution to the overall solution variability, while the local analysis identifies the dependence of the solution on each parameter in the small neighborhood of its nominal value. To construct the PC expansions, here of total degree three, we used a regression approach based

on ℓ_1 -minimization (54–56) using 250 randomly sampled parameter sets, and the corresponding realizations of $\langle\tau_c\rangle$ and $\langle L\rangle$. In figs. 3 and 4–6 below, each point corresponds to one of the 250 parameter sets.

Effects of varying mean MT length

The rotational diffusion coefficient of a rod varies as L^{-3} , making MT length important for KC capture by a fixed-length MT (24). We found that the MT mean length was also important for KC capture with dynamic instability. Indeed, the primary determinant of the capture time was the mean MT length (fig. 3), for all models studied. The capture time decreased by approximately a factor of 10 as $\langle L\rangle$ increased from short ($\lesssim 0.3 \mu\text{m}$) to long ($\gtrsim 1.5 \mu\text{m}$, half the nuclear diameter). A longer MT increases the effective number of binding sites for a KC, lowering the capture time. If the number of binding sites were the sole factor determining the rate of KC capture, we would expect $\langle\tau_c\rangle \sim \langle L\rangle^{-1}$. The dependence in our model is more complex, because the MT dynamics also change with $\langle L\rangle$. Nevertheless, fitting the capture time as a function of the mean length to the form $\langle\tau_c\rangle = A\langle L\rangle^{-1} + B$ (solid lines in fig. 3) gave reasonable agreement with our simulation results.

For all MT lengths and both slow and fast dynamic instability, adding MT rotational diffusion to a model with only dynamic instability reduced the capture time. The contribution of rotational diffusion depended on the MT dynamics: $\langle\tau_c\rangle$ decreased by 23% on average (25% at most) for the slow model, and by 9% on average (16% at most) for the fast model. The speed up due to rotational diffusion was larger for slower MT dynamics and shorter MTs (fig. 3). For the most relevant MT lengths in fission yeast of around $1 \mu\text{m}$, rotational diffusion shortened the capture time by at most 14% for the slow model and 6% for the fast model. This suggests that while rotational diffusion does speed up KC capture, it makes a relatively small quantitative contribution, consistent with recent work (27).

Sensitivity analysis

We performed sensitivity analysis to check how the capture time and MT mean length vary with model parameters. For dynamic instability with no boundary effects, we would expect a mean length of $\langle L\rangle = v_g/f_{+0}$ in the slow model and $\langle L\rangle = v_g v_s / (v_s f_c - v_g f_r) \approx v_g / f_c$ in the fast model ((51) and Supporting Material). While interactions of MTs with the nuclear envelope alter this relationship, we expected that the MT mean length and therefore the capture time depend primarily on the MT growth speed and the catastrophe frequency (or its analogue in the slow model, the grow-to-pause frequency).

To test these relationships, we performed a global sensitivity analysis of the mean capture time and MT length to the dynamic instability parameters using the analysis of the variance of $\langle\tau_c\rangle$ and $\langle L\rangle$ based on the so-called Sobol’ decomposition (57), which we computed directly using the PC expansion ((58) and Supporting Material). The PC expansion gave low errors of a few percent (table S2), indicating that it accurately describes the full simulation model. As expected, $\langle\tau_c\rangle$ and $\langle L\rangle$ are most sensitive to the growth speed and effective catastrophe frequency, and this dependence is not altered significantly by the addition of rotational diffusion to the model (table S3). We also determined the local sensitivity of the capture time to these parameters (Supporting Material, fig. S3).

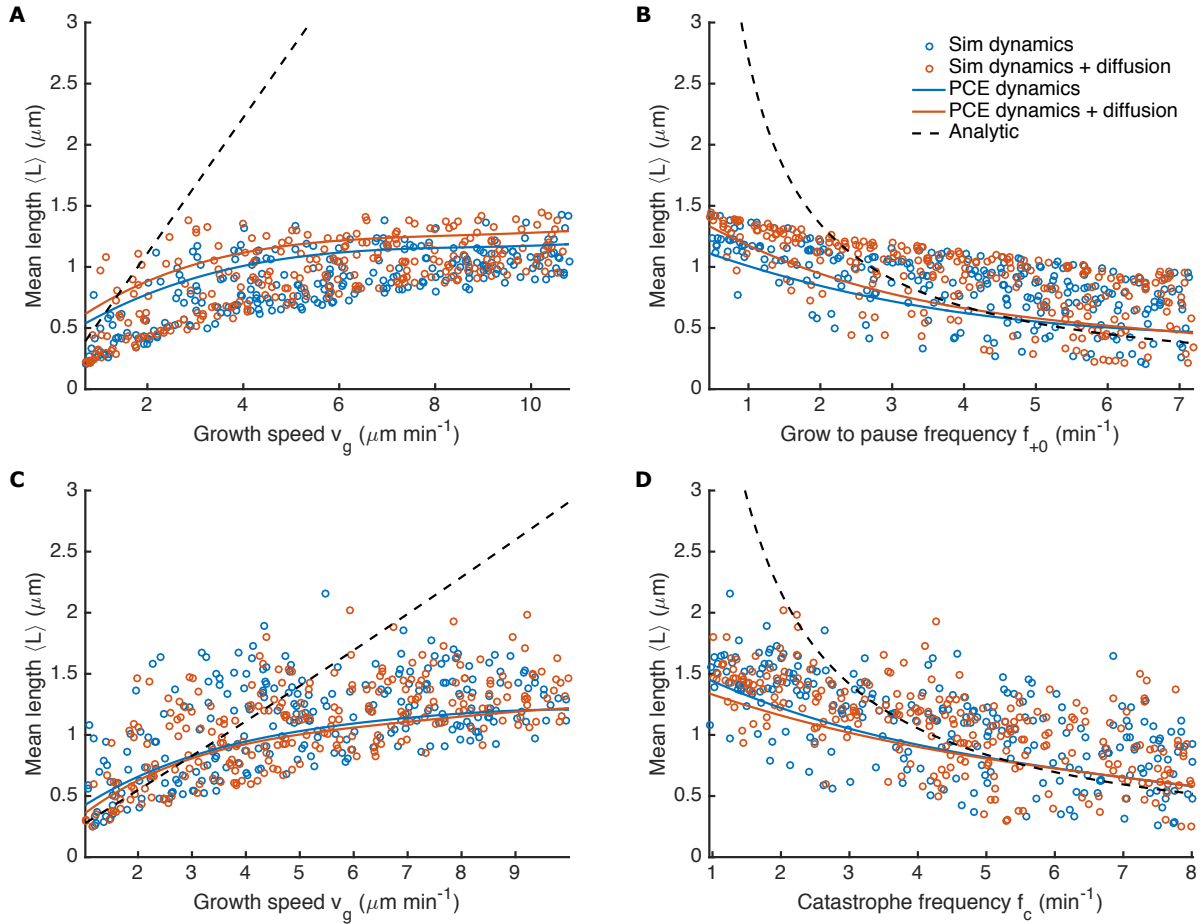


Figure 4: Variation of microtubule length with single parameters. (A, B) Slow model. (C, D) Fast model. Points represent individual simulations of model with dynamic instability only (blue) and model with dynamic instability and rotational diffusion (orange). Solid lines indicate a projection of the polynomial chaos expansion prediction in one dimension for variation of indicated parameter with other parameters at their reference values. Dashed line indicates predicted mean microtubule length for dynamic instability in the absence of boundary effects.

Variation with individual parameters

To develop better intuition for how variation of individual parameters affects capture, we used both our individual simulations and the PC expansion to study how the MT mean length and capture time depend on variation of individual parameters (figs. 4, S4, S5). The solid lines are the predicted dependence of $\langle L \rangle$ for the reference parameter set on the varied single parameter from the PC expansion, while the dashed line is the analytic prediction for $\langle L \rangle$ with unconstrained dynamic instability. As expected, the analytic solution that neglects boundary interactions matches the data and PC expansion well when $\langle L \rangle$ is relatively small, but differs significantly where $\langle L \rangle \gtrsim 1 \mu\text{m}$. The points show the behavior of individual simulations with widely varying parameters, illustrating the range of behavior of our model.

The variation of the capture time with individual parameters show qualitatively similar dependence (figs. 5, S4, S5). Consistent with intuitive expectations, parameter sets with higher growth speed and lower catastrophe frequency lead to shorter capture times. Growth speed is the main parameter affecting capture time, causing it to vary by up to a factor of five, consistent with its total Sobol' index (table S3). This makes sense because MTs with higher growth speeds search a

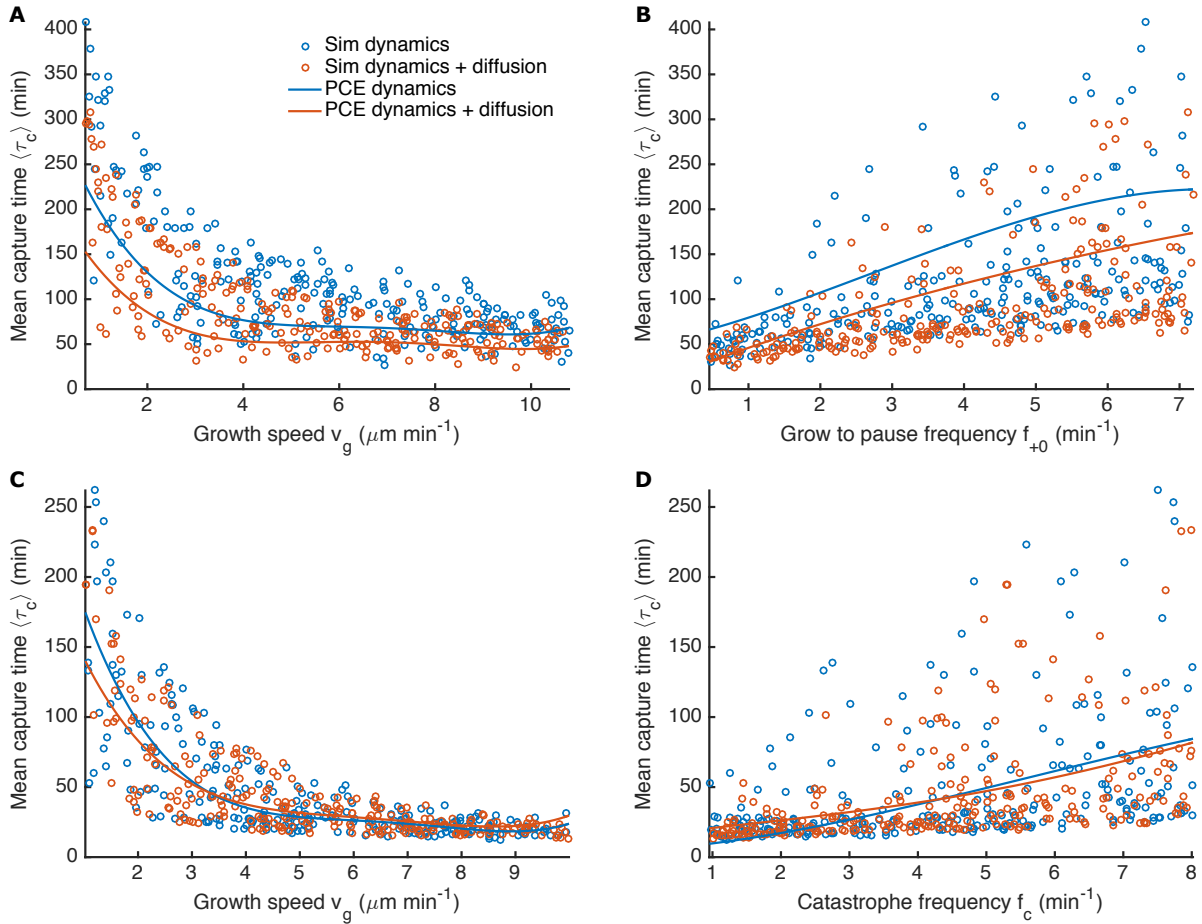


Figure 5: Variation of capture time with single parameters. (A, B) Slow model. (C, D) Fast model. Points represent individual simulations of model with dynamic instability only (blue) and model with dynamic instability and rotational diffusion (orange). Solid lines indicate a projection of the polynomial chaos expansion prediction in one dimension for variation of indicated parameter with other parameters at their reference values.

given direction more quickly than slower MTs with the same orientation, resulting in lower capture time; fast-growing MTs have also typically longer mean lengths. Also as expected, catastrophe frequency affects the capture time, because high catastrophe frequency tends to reduce the mean length of MTs. However, MTs with low catastrophe frequency typically reach the nuclear envelope and undergo force-induced catastrophe, which limits the advantage gained by lowering the catastrophe frequency. The shrinking speed and rescue frequency have little effect on the capture time, because they don't significantly affect the mean MT length (figs. S4, S5). For simulations both with and without MT rotational diffusion, varying these parameters alone varies the capture time by $\lesssim 25\%$.

Lateral versus end-on capture

In fission yeast, KC capture occurs primarily via end-on attachment, with about 75% of captures occurring < 500 nm away from the MT tip (24), while other other work both in large and small cells has found a high frequency of lateral attachments (14, 19, 20, 23, 25). In our model, we classified attachments as end-on if the capture occurred within $4.5\sigma_{MT}$ (≈ 113 nm) from the MT

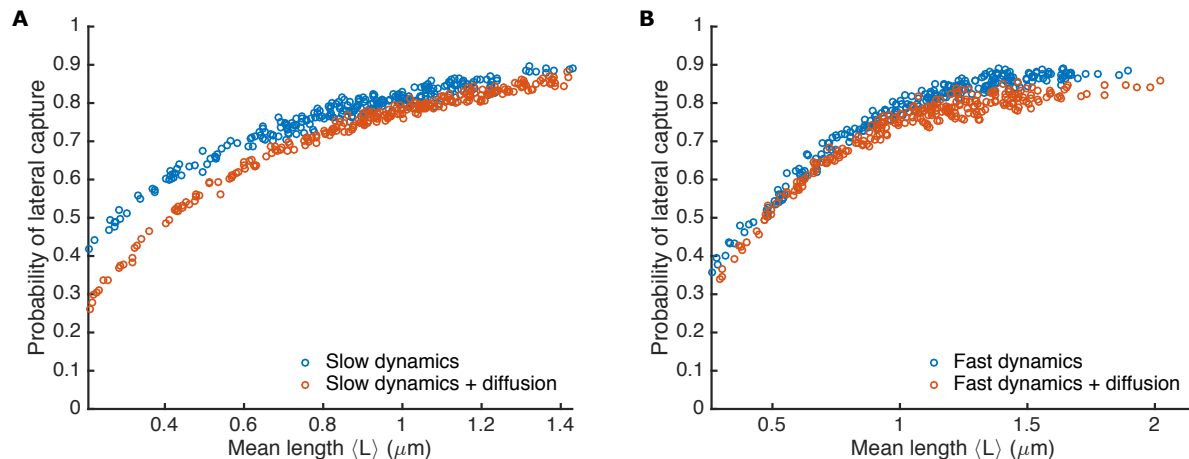


Figure 6: The fraction of captures that occur laterally as a function of mean microtubule length. (A) Slow model. (B) Fast model. Points represent individual simulations of model with dynamic instability only (blue) and model with dynamic instability and rotational diffusion (orange).

tip, and lateral otherwise. We found that lateral attachments are more likely in our model, but the fraction of captures that occur laterally depends on the mean MT length (fig. 6). Increasing $\langle L \rangle$ increased the probability of lateral capture, because the available MT surface area for binding laterally increases.

Remarkably, we found that lateral captures predominated even in the model with dynamic instability only (no rotational diffusion). This occurred for two reasons: first, interactions of MTs with the nuclear envelope caused some MT reorientation in the absence of thermal diffusion. However, we observed significant lateral attachment even for relatively short MTs that didn't interact with the nuclear envelope, because KC diffusion allowed lateral attachment even for fixed-orientation MTs.

Surprisingly, adding rotational diffusion to the model made end-on attachments more likely: diffusion *decreases* the probability of lateral capture, an effect that was more noticeable for shorter MTs. Rotational diffusion allows the MT to sweep through space, increasing the volume searched by the MT. This increase in effective volume searched is largest at the MT tip because the tip is furthest from the pivot point at the SPB. This effect was more important for shorter MTs where end-on attachments were more likely.

It's not clear why our model found primarily lateral captures, while Kalinina et al. (24) measured primarily end-on captures. Some difference would be expected due to the different definitions of end-on versus lateral attachment: Kalinina et al. used a 500-nm distance cutoff that was limited by optical resolution. In addition, it is possible that because lost KCs were induced by a short cold treatment in these experiments, more of the KCs were close to the SPB and were captured by shorter MTs for which rotational diffusion is more important.

Conclusions

The search-and-capture model has been considered the main mechanism by which KCs are captured since the discovery of MT dynamic instability (9, 11–13). The original picture of search and capture posited that MTs undergo dynamic instability nucleated from centrosomes until they form end-on attachments with KCs. Additional effects such as diffusion of KCs, (12, 15), a bias in MT

growth toward chromosomes (16–18), MT nucleation from KCs (15, 21, 22), spatial distribution and rotation of chromosomes (15, 19, 20), and KC size decreases after capture (20) can make search and capture more rapid. MT rotational diffusion and lateral capture were found to be important mechanisms in fission yeast (24). This work suggested that MT rotational diffusion about centrosomes is important, but because the model assumed fixed-length MTs it was unable to directly evaluate the relative importance of rotational diffusion and dynamic instability to KC capture.

We developed a biophysical model of KC capture in fission yeast that includes MT dynamic instability and rotational diffusion, KC diffusion, and interactions with the nuclear envelope (fig. 1). We used the model to compare the time course of KC capture in models with and without MT rotational diffusion. The mitotic MTs measured by Kalinina *et al.* were primarily paused (24), and the measured dynamics appeared slow compared to previous measurements (32). Therefore, we performed further measurements of the dynamics of MTs in fission yeast monopolar spindles with low-level fluorescent tubulin labeling. We found more rapid dynamic instability of single MTs, with little pausing (fig. 2). This motivated us to consider two dynamic instability models: a slow model with dynamics measured by Kalinina *et al.*, and a fast model with dynamics measured in this work (table 1).

We studied KC capture by single MTs in our model both for the reference parameter sets and for broad ranges of parameters around the reference sets. In all cases, KC capture occurred more quickly when rotational diffusion about SPBs was added to a model with only dynamic instability (fig. 3): $\langle \tau_c \rangle$ decreased by 23% on average for the slow model, and by 9% on average for the fast model, similar to recent work (27). We found that the primary determinant of the capture time was the mean MT length. Longer MTs have a larger surface on which the KC can bind, which suggests that the capture time $\langle \tau_c \rangle \sim \langle L \rangle^{-1}$, as we observed. Since the MT growth speed and catastrophe frequency controlled the mean length in the parameter regimes we studied, these parameters had the biggest effect on the capture time (table S3, fig. S3).

For the experimentally measured mitotic polar MT lengths of $\sim 1 \mu\text{m}$ in fission yeast, adding rotational diffusion to our model shortened the capture time by 14% for the slow model and 6% for the fast model. This suggests that rotational diffusion causes relatively small changes to the capture time for typical conditions in fission yeast. We note that our model, like that of Kalinina *et al.* (24) considered the capturing MT only and neglected the bipolar spindle that assembles in prometaphase and the possibility of capturing MTs from the other spindle-pole body. Because the assembled spindle alters the rotational freedom of mitotic polar MTs, in future work it would be interesting to study how the presence of the spindle affects the kinetics of KC capture.

We further examined how MT length (fig. 4) and capture time (fig. 5) varied with the growth speed and catastrophe frequency. The mean length varied qualitatively as expected from the predictions of analytic theory that neglects MT interactions with the nuclear envelope. In the computational model, changes from this theory became significant for longer MTs. Parameter sets with higher growth speed and lower catastrophe frequency that lead to longer mean MT lengths had shorter capture times.

The original search-and-capture model supposed that KC attachments to MTs are end on, consistent with the results of Kalinina *et al.* (24), while others observed primarily lateral attachments (14, 19, 20, 23, 25). Therefore, we studied how the probability of lateral or end-on attachment varied with MT length and the presence or absence of rotational diffusion in the model (fig. 6). Lateral captures predominated, even in the absence of MT rotational diffusion. Somewhat counterintuitively, we found that adding rotational diffusion to the model made end-on attachments more likely. A diffusing MT searches a larger volume of space than a rotationally constrained MT, an effect which is largest for the MT tip. Therefore, rotational diffusion can decrease lateral

attachment.

Recently, Magidson et al. proposed that initial lateral contacts are important to the timing and low error rates of KC-spindle attachment in human cells (20). Although many proteins are known to contribute to KC-MT attachment, including motors and non-motor MT-binding proteins (the Ndc80 complex, other components of the KMN network, Ska or Dam1, and others) (59), the contributions of end-on versus lateral KC-MT attachment pathways are not fully understood. Our work suggests that lateral captures are enhanced when MT rotational diffusion about SPBs is decreased or eliminated, as would be the case in large spindles with many long MTs. Future work dissecting contributions of lateral and end-on attachment mechanisms may contribute interesting additional insights into this biologically important problem.

Author contributions

RB, OS-S, CE, ZRG, AD, JRM, MAG, and MDB designed research; RB, OS-S, CE, ZRG, PJF, SM, AC, and MDB performed research; RB, OS-S, CE, ZRG, PJF, AD, MAG, and MDB contributed analytic tools; RB, OS-S, CE, ZRG, PJF, SM, AC, and MDB analyzed data; RB, CE, ZRG, PJF, and MDB wrote the manuscript.

Acknowledgements

We thank Iain Hagan and Jonathan Millar for providing fission yeast strains, Keith Gull for providing the TAT-1 antibody, and Nenad Pavin for useful discussions. This work was supported by NSF grants DMR-0847685 and DMR-1551095 to MDB, MRSEC DMR-0820579 and DMR-1420736 to MAG, and CMMI-1454601 to AD; and NIH grants K25 GM110486 to MDB and R01 GM033787 to JRM. This work utilized the Janus supercomputer, which is supported by the National Science Foundation (CNS-0821794), the University of Colorado Boulder, the University of Colorado Denver, and the National Center for Atmospheric Research. The Janus supercomputer is operated by the University of Colorado Boulder.

References

1. McIntosh, J. R., M. I. Molodtsov, and F. I. Ataullakhanov, 2012. Biophysics of mitosis. *Quarterly Reviews of Biophysics* 45:147–207.
2. Cottingham, F. R., and M. A. Hoyt, 1997. Mitotic spindle positioning in *Saccharomyces cerevisiae* is accomplished by antagonistically acting microtubule motor proteins. *The Journal of Cell Biology* 138:1041–1053.
3. Goshima, G., and R. D. Vale, 2003. The roles of microtubule-based motor proteins in mitosis. *The Journal of Cell Biology* 162:1003–1016.
4. Grishchuk, E. L., and J. R. McIntosh, 2006. Microtubule depolymerization can drive poleward chromosome motion in fission yeast. *The EMBO Journal* 25:4888–4896.
5. Schroer, T. A., 2001. Microtubules don and doff their caps: dynamic attachments at plus and minus ends. *Current Opinion in Cell Biology* 13:92–96.

6. Garcia, M. A., N. Koonrugsa, and T. Toda, 2002. Spindle–kinetochore attachment requires the combined action of Kin I-like Klp5/6 and Alp14/Dis1-MAPs in fission yeast. *The EMBO Journal* 21:6015.
7. Akhmanova, A., and M. O. Steinmetz, 2008. Tracking the ends: a dynamic protein network controls the fate of microtubule tips. *Nature Reviews Molecular Cell Biology* 9:309–322.
8. Duesberg, P., R. Li, A. Fabarius, and R. Hehlmann, 2006. Aneuploidy and cancer: from correlation to causation. In T. Dittmar, K. S. Zaenker, and A. Schmidt, editors, *Infection and Inflammation: Impacts on Oncogenesis*, Karger, Basel, volume 13 of *Contrib Microbiol*, 16–44.
9. Mitchison, T., and M. Kirschner, 1984. Dynamic instability of microtubule growth. *Nature* 312:237–242.
10. Mitchison, T. J., and M. W. Kirschner, 1985. Properties of the kinetochore in vitro. II. Microtubule capture and ATP-dependent translocation. *The Journal of Cell Biology* 101:766–777.
11. Hill, T. L., 1985. Theoretical problems related to the attachment of microtubules to kinetochores. *Proceedings of the National Academy of Sciences* 82:4404–4408.
12. Holy, T. E., and S. Leibler, 1994. Dynamic instability of microtubules as an efficient way to search in space. *Proceedings of the National Academy of Sciences* 91:5682–5685.
13. Heald, R., and A. Khodjakov, 2015. Thirty years of search and capture: The complex simplicity of mitotic spindle assembly. *The Journal of Cell Biology* 211:1103–1111.
14. Rieder, C. L., and S. P. Alexander, 1990. Kinetochores are transported poleward along a single astral microtubule during chromosome attachment to the spindle in newt lung cells. *The Journal of Cell Biology* 110:81–95.
15. Paul, R., R. Wollman, W. T. Silkworth, I. K. Nardi, D. Cimini, and A. Mogilner, 2009. Computer simulations predict that chromosome movements and rotations accelerate mitotic spindle assembly without compromising accuracy. *Proceedings of the National Academy of Sciences* 106:15708–15713.
16. Carazo-Salas, R. E., G. Guarguaglini, O. J. Gruss, A. Segref, E. Karsenti, and I. W. Mattaj, 1999. Generation of GTP-bound Ran by RCC1 is required for chromatin-induced mitotic spindle formation. *Nature* 400:178–181.
17. Wollman, R., E. Cytrynbaum, J. Jones, T. Meyer, J. Scholey, and A. Mogilner, 2005. Efficient Chromosome Capture Requires a Bias in the ‘Search-and-Capture’ Process during Mitotic Spindle Assembly. *Current Biology* 15:828–832.
18. O’Connell, C. B., J. Lončarek, P. Kaláb, and A. Khodjakov, 2009. Relative contributions of chromatin and kinetochores to mitotic spindle assembly. *The Journal of Cell Biology* 187:43–51.
19. Magidson, V., C. B. O’Connell, J. Lončarek, R. Paul, A. Mogilner, and A. Khodjakov, 2011. The Spatial Arrangement of Chromosomes during Prometaphase Facilitates Spindle Assembly. *Cell* 146:555–567.
20. Magidson, V., R. Paul, N. Yang, J. G. Ault, C. B. O’Connell, I. Tikhonenko, B. F. McEwen, A. Mogilner, and A. Khodjakov, 2015. Adaptive changes in the kinetochore architecture facilitate proper spindle assembly. *Nature Cell Biology* .

21. Witt, P. L., H. Ris, and G. G. Borisy, 1980. Origin of kinetochore microtubules in Chinese hamster ovary cells. *Chromosoma* 81:483–505.
22. Kitamura, E., K. Tanaka, S. Komoto, Y. Kitamura, C. Antony, and T. U. Tanaka, 2010. Kinetochores Generate Microtubules with Distal Plus Ends: Their Roles and Limited Lifetime in Mitosis. *Developmental Cell* 18:248–259.
23. Tanaka, K., N. Mukae, H. Dewar, M. van Breugel, E. K. James, A. R. Prescott, C. Antony, and T. U. Tanaka, 2005. Molecular mechanisms of kinetochore capture by spindle microtubules. *Nature* 434:987–994.
24. Kalinina, I., A. Nandi, P. Delivani, M. R. Chacón, A. H. Klemm, D. Ramunno-Johnson, A. Krull, B. Lindner, N. Pavin, and I. M. Tolić-Norrelykke, 2012. Pivoting of microtubules around the spindle pole accelerates kinetochore capture. *Nature Cell Biology* .
25. Kitajima, T. S., M. Ohsugi, and J. Ellenberg, 2011. Complete Kinetochore Tracking Reveals Error-Prone Homologous Chromosome Biorientation in Mammalian Oocytes. *Cell* 146:568–581.
26. Gopalakrishnan, M., and B. S. Govindan, 2011. A First-Passage-Time Theory for Search and Capture of Chromosomes by Microtubules in Mitosis. *Bulletin of Mathematical Biology* 73:2483–2506.
27. Cojoc, G., A.-M. Florescu, A. Krull, A. H. Klemm, N. Pavin, F. Jülicher, and I. M. Tolić, 2016. Paired arrangement of kinetochores together with microtubule pivoting and dynamics drive kinetochore capture in meiosis I. *Scientific Reports* 6:25736.
28. Gao, T., R. Blackwell, M. A. Glaser, M. D. Betterton, and M. J. Shelley, 2015. Multiscale modeling and simulation of microtubule-motor-protein assemblies. *Physical Review E* 92:062709.
29. Gao, T., R. Blackwell, M. A. Glaser, M. Betterton, and M. J. Shelley, 2015. Multiscale Polar Theory of Microtubule and Motor-Protein Assemblies. *Physical Review Letters* 114:048101.
30. Kuan, H.-S., R. Blackwell, L. E. Hough, M. A. Glaser, and M. D. Betterton, 2015. Hysteresis, reentrance, and glassy dynamics in systems of self-propelled rods. *Physical Review E* 92:060501.
31. Blackwell, R., O. Sweezy-Schindler, C. Baldwin, L. E. Hough, M. A. Glaser, and M. D. Betterton, 2016. Microscopic origins of anisotropic active stress in motor-driven nematic liquid crystals. *Soft Matter* .
32. Sagolla, M. J., S. Uzawa, and W. Z. Cande, 2003. Individual microtubule dynamics contribute to the function of mitotic and cytoplasmic arrays in fission yeast. *Journal of Cell Science* 116:4891–4903.
33. Laan, L., N. Pavin, J. Husson, G. Romet-Lemonne, M. van Duijn, M. P. López, R. D. Vale, F. Jülicher, S. L. Reck-Peterson, and M. Dogterom, 2012. Cortical Dynein Controls Microtubule Dynamics to Generate Pulling Forces that Position Microtubule Asters. *Cell* 148:502–514.
34. Pavin, N., L. Laan, R. Ma, M. Dogterom, and F. Jülicher, 2012. Positioning of microtubule organizing centers by cortical pushing and pulling forces. *New Journal of Physics* 14:105025.
35. Ma, R., L. Laan, M. Dogterom, N. Pavin, and F. Jülicher, 2014. General theory for the mechanics of confined microtubule asters. *New Journal of Physics* 16:013018.

36. Tischer, C., D. Brunner, and M. Dogterom, 2009. Force- and kinesin-8-dependent effects in the spatial regulation of fission yeast microtubule dynamics. *Molecular Systems Biology* 5:1–10.
37. Dogterom, M., and B. Yurke, 1997. Measurement of the Force-Velocity Relation for Growing Microtubules. *Science* 278:856–860.
38. Janson, M. E., M. E. de Dood, and M. Dogterom, 2003. Dynamic instability of microtubules is regulated by force. *The Journal of Cell Biology* 161:1029–1034.
39. Yamagishi, Y., C. H. Yang, Y. Tanno, and Y. Watanabe, 2012. MPS1/Mph1 phosphorylates the kinetochore protein KNL1/Spc7 to recruit SAC components. *Nature Cell Biology* 14:746–752.
40. Hagan, I., and M. Yanagida, 1990. Novel potential mitotic motor protein encoded by the fission yeast *cut7+* gene. *Nature* 347:563–566.
41. Costa, J., C. Fu, V. Syrovatkina, and P. T. Tran, 2013. Chapter 24 - Imaging Individual Spindle Microtubule Dynamics in Fission Yeast. In J. J. C. Wilson, and Leslie, editors, *Methods in Cell Biology*, Academic Press, volume 115 of *Microtubules, in Vitro*, 385–394.
42. Demchouk, A. O., M. K. Gardner, and D. J. Odde, 2011. Microtubule Tip Tracking and Tip Structures at the Nanometer Scale Using Digital Fluorescence Microscopy. *Cellular and Molecular Bioengineering* 4:192–204.
43. Prahl, L. S., B. T. Castle, M. K. Gardner, and D. J. Odde, 2014. Chapter Three - Quantitative Analysis of Microtubule Self-assembly Kinetics and Tip Structure. In R. D. Vale, editor, *Methods in Enzymology*, Academic Press, volume 540 of *Reconstituting the Cytoskeleton*, 35–52.
44. Ding, R., K. L. McDonald, and J. R. McIntosh, 1993. Three-dimensional reconstruction and analysis of mitotic spindles from the yeast, *Schizosaccharomyces pombe*. *The Journal of Cell Biology* 120:141–151.
45. Alberts, B., A. Johnson, J. Lewis, M. Raff, K. Roberts, and P. Walter, 2008. *Molecular Biology of the Cell*. Garland, New York, 5th edition.
46. Snaith, H. A., A. Anders, I. Samejima, and K. E. Sawin, 2010. Chapter 9 - New and Old Reagents for Fluorescent Protein Tagging of Microtubules in Fission Yeast: Experimental and Critical Evaluation. In Lynne Cassimeris and Phong Tran, editor, *Methods in Cell Biology*, Academic Press, volume Volume 97, 147–172.
47. Bratman, S. V., and F. Chang, 2007. Stabilization of Overlapping Microtubules by Fission Yeast CLASP. *Developmental Cell* 13:812–827.
48. Bratman, S. V., and F. Chang, 2008. Mechanisms for maintaining microtubule bundles. *Trends in Cell Biology* 18:580–586.
49. Fygenson, D. K., E. Braun, and A. Libchaber, 1994. Phase diagram of microtubules. *Physical Review E* 50:1579.
50. Gardner, M. K., D. C. Bouck, L. V. Paliulis, J. B. Meehl, E. T. O’Toole, J. Haase, A. Soubry, A. P. Joglekar, M. Winey, E. D. Salmon, K. Bloom, and D. J. Odde, 2008. Chromosome Congression by Kinesin-5 Motor-Mediated Disassembly of Longer Kinetochore Microtubules. *Cell* 135:894–906.

51. Dogterom, M., and S. Leibler, 1993. Physical aspects of the growth and regulation of microtubule structures. *Physical Review Letters* 70:1347–1350.
52. Ghanem, R., and P. Spanos, 2002. Stochastic Finite Elements: A Spectral Approach. Dover.
53. Xiu, D., and G. Karniadakis, 2002. The Wiener-Askey polynomial chaos for stochastic differential equations. *SIAM Journal on Scientific Computing* 24:619–644.
54. Doostan, A., and H. Owhadi, 2011. A non-adapted sparse approximation of PDEs with stochastic inputs. *Journal of Computational Physics* 230:3015–3034.
55. Hampton, J., and A. Doostan, 2015. Compressive sampling of polynomial chaos expansions: Convergence analysis and sampling strategies. *Journal of Computational Physics* 280:363 – 386.
56. Hadigol, M., K. Maute, and A. Doostan, 2015. On uncertainty quantification of lithium-ion batteries: Application to an LiC₆/LiCoO₂ cell. *Journal of Power Sources* 300:507–524.
57. Sobol', I., 1990. On sensitivity estimation for nonlinear mathematical models. *Matematicheskoe Modelirovanie* 2:112–118.
58. Sudret, B., 2008. Global sensitivity analysis using polynomial chaos expansions. *Reliability Engineering and System Safety* 93:964 – 979.
59. Cheeseman, I. M., and A. Desai, 2008. Molecular architecture of the kinetochore–microtubule interface. *Nature Reviews Molecular Cell Biology* 9:33–46.
60. Lowen, H., 1994. Brownian dynamics of hard spherocylinders. *Physical Review E* 50:1232–1242.
61. Weeks, J. D., D. Chandler, and H. C. Andersen, 1971. Role of Repulsive Forces in Determining the Equilibrium Structure of Simple Liquids. *The Journal of Chemical Physics* 54:5237–5247.
62. Moreno, S., A. Klar, and P. Nurse, 1991. Molecular genetic analysis of fission yeast *Schizosaccharomyces pombe*. In *Guide to Yeast Genetics and Molecular Biology*, Academic Press, volume Volume 194, 795–823.

Supporting Material

1 Model

MTs are rigid spherocylinders (cylinders with hemispherical ends) with length $L(t)$ and diameter σ_{MT} . One end of the MT is fixed to a point on the nuclear envelope. The equations of motion for microtubule reorientation are

$$\mathbf{u}_i(t + \delta t) = \mathbf{u}_i(t) + \frac{D_\theta(L)}{k_B T} \mathbf{T}_i(t) \times \mathbf{u}_i(t) \delta t + \delta \mathbf{u}_i(t), \quad (\text{S1})$$

where $D_\theta(L)$ is the rotational diffusion coefficient, $\mathbf{T}_i(t)$ is the systematic torque on particle i , and the random reorientation $\delta \mathbf{u}_i(t)$ is Gaussian-distributed, with variance $\langle \delta \mathbf{u}_i(t) \delta \mathbf{u}_i(t) \rangle = 2D_\theta(L) [\mathbf{I} - \mathbf{u}_i(t) \mathbf{u}_i(t)] \delta t$. MTs have a length-dependent rotational diffusion coefficient $D_\theta(L) \sim L^{-3}$. Using the formula for spherocylinder rotational diffusion from Löwen *et al.* (60), we calculated $D_\theta(L)$ for each timestep of the simulation:

$$D_\theta(L(t)) = \frac{3k_b T}{\pi \eta (L(t) + 1)^3} (\ln a_{MT} - 0.662 + 0.917/a_{MT} - 0.050/a_{MT}^2), \quad (\text{S2})$$

where η is the fluid viscosity, and $a_{MT} = L(t)/\sigma_{MT}$.

The MT minimum length is $4 \sigma_{MT}$. We tested shorter minimum lengths, but found that decreasing below $4 \sigma_{MT}$ did not significantly change the capture time; this choice of minimum length makes the simulations more stable.

KCs are spheres with diameter σ_{KC} and diffusion coefficient D_{kc} (Table 1) that obey the equation of motion

$$\mathbf{r}_i(t + \delta t) = \mathbf{r}_i(t) + \frac{D_{kc}}{k_B T} \mathbf{F}_i(t) + \delta \mathbf{r}_i(t), \quad (\text{S3})$$

with Gaussian random displacements with variance $\langle \delta \mathbf{r}_i(t) \delta \mathbf{r}_i(t) \rangle = 2D_{kc} \delta t$.

To account for variations in the relative diffusion of KCs and MTs, we defined the MT and KC diffusion coefficients independently (fig. S1). We nondimensionalized the parameters using the reference length σ_{MT} of a MT diameter (25 nm), and the reference diffusion coefficient D_0 ; these together determine the unit of time $\tau = \sigma_{MT}^2/D_0$. A kinetochore of size 200nm has a diffusion constant of $D_{kc} = 5.9 \times 10^{-4} \mu\text{m}^2 \text{ s}^{-1}$. Using Stokes calculation for D, we see that $D_{kc} = \frac{1}{8} D_0$, yielding $D_0 = 4.72 \times 10^{-3} \mu\text{m}^2 \text{ s}^{-1}$.

1.1 Boundary interactions

To ensure that MTs and KCs remained within the nuclear envelope, both MT free ends and KCs interacted with the envelope via the Weeks-Chandler-Anderson potential (61)

$$u_{\text{wca,fil}}(r_{\text{min}}) = \begin{cases} 4k_B T \left[\left(\frac{\sigma}{r_{\text{min}}} \right)^{12} - \left(\frac{\sigma}{r_{\text{min}}} \right)^6 \right] + k_B T, & r_{\text{min}} < 2^{1/6} \sigma \\ 0, & r_{\text{min}} \geq 2^{1/6} \sigma, \end{cases} \quad (\text{S4})$$

where r_{min} is minimum distance between the free end of the filament and the enclosing sphere with radius $R + \sigma/2$, and σ is the finite distance at which the potential goes to zero. This allows for smooth continuation of the dynamics at the boundary; the nuclear envelope then has an effective radius of R .

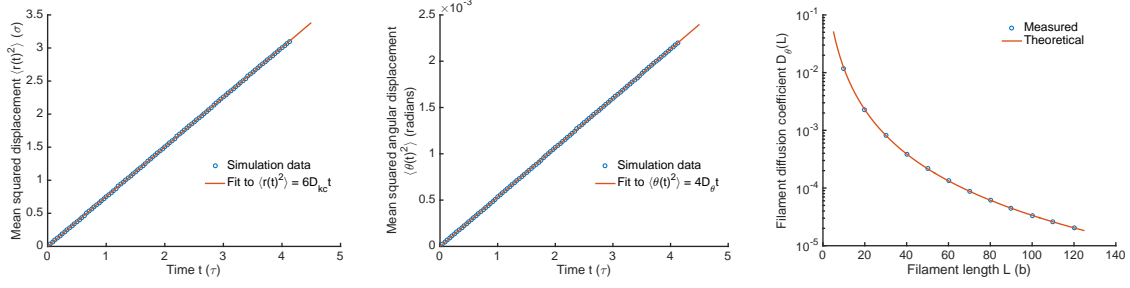


Figure S1: Diffusion coefficient verification. (a) Kinetochore mean-squared displacement versus time for a $0.2 \mu\text{m}$ diameter kinetochore. Points indicate measured values from a simulation with no boundary; The line is a linear fit of $\langle r(t)^2 \rangle = 6D_{kc}t$. (b) Filament mean-squared angular displacement versus time. Points indicate measured values from a simulation with no boundary. The line is a linear fit of $\langle \theta(t)^2 \rangle = 4D_\theta t$. (c) Rotational diffusion coefficients versus microtubule length for filaments of fixed length. Points are measured values from a simulation with no boundary. The line is the diffusion coefficient from Löwen et al. (60). Values in all plots are in dimensionless simulation units.

Kinetochores have a similar interaction with the envelope

$$u_{\text{wca},\text{kc}}(r_{\min}) = \begin{cases} 4k_B T \left[\left(\frac{\sigma_{\text{kc}}/2 + \sigma/2}{r_{\min}} \right)^{12} - \left(\frac{\sigma_{\text{kc}}/2 + \sigma/2}{r_{\min}} \right)^6 \right] + k_B T, & r_{\min} < 2^{1/6}(\sigma_{\text{kc}} + \sigma)/2 \\ 0, & r_{\min} \geq 2^{1/6}(\sigma_{\text{kc}} + \sigma)/2, \end{cases} \quad (\text{S5})$$

where again an enclosing boundary is a sphere with radius $R + \sigma/2$.

1.2 Dynamic instability models

We consider two dynamic instability models. The first is the original two-state dynamic instability model of Dogterom and Leibler (51). The microtubule (MT) grows (shrinks) at a constant velocity v_g (v_s), with transition frequencies f_c (f_r) to the other state. This leads to an exponential distribution of MT lengths in the bounded growth regime, with mean length

$$\langle L \rangle = \frac{v_g v_s}{v_s f_c - v_g f_r}. \quad (\text{S6})$$

If the second term in the denominator is small, which commonly occurs in cells when the rescue frequency is low, we have $v_g f_r \ll v_s f_c$ and this becomes approximately

$$\langle L \rangle \approx \frac{v_g}{f_c}. \quad (\text{S7})$$

1.2.1 Slow dynamic instability

We consider MTs that can be in 3 states: growing, shrinking, or pausing. In the paused state, the MT length doesn't change with time. As in previous work, we consider the probability distribution of MT state and length $P_s(z, t)$, where s labels the state (+, -, and 0 label growing, shrinking, and pausing states), z length, and t time. The equations of the three-state model are

$$\frac{\partial P_+(z, t)}{\partial t} = -f_{+0}P_+ + f_{0+}P_0 - v_g \frac{\partial P_+}{\partial z}, \quad (\text{S8})$$

$$\frac{\partial P_-(z, t)}{\partial t} = -f_{-0}P_- + f_{0-}P_0 + v_s \frac{\partial P_-}{\partial z}, \quad (\text{S9})$$

$$\frac{\partial P_0(z, t)}{\partial t} = -(f_{0-} + f_{0+})P_0 + f_{+0}P_+ + f_{-0}P_-. \quad (\text{S10})$$

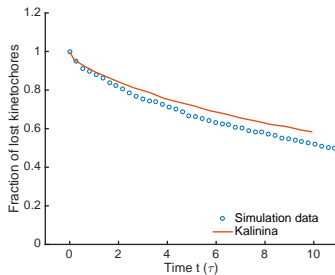


Figure S2: Comparison of fraction of lost kinetochores versus time in our model to those of Kalinina et al. (24). For this comparison, we inserted kinetochores in the the nucleus uniformly $1.2 \mu m$ from the base of the filament to mimic the approach of Kalinina et al. Microtubules were inserted with uniform angles that did not cause overlap with the boundary. The difference between the two models is likely due to the overlap criteria: Kalinina et al used an approximate angular criterion to detect overlaps that did not account for the non-zero volume of the filament (24). This effectively decreased the capture radius compared to our model.

Here f_{+0} is the frequency of transitions from the growing state to the paused state, and so on. To determine the mean length $\langle L \rangle$, we study the steady state equations. After summing the steady state equations, the state switching terms cancel and we have

$$v_+ \frac{\partial P_+}{\partial z} = v_- \frac{\partial P_-}{\partial z}. \quad (\text{S11})$$

Integrating both sides of the equation with respect to z and setting the integration constant to 0 (as required for a bounded length distribution for which the probability density goes to zero for large z) gives

$$P_- = \frac{v_+}{v_-} P_+. \quad (\text{S12})$$

Similarly, the steady-state of equation (S10) gives

$$P_0 = \left(\frac{f_{+0} + v_+ f_{-0}/v_-}{f_{0+} + f_{0-}} \right) P_+. \quad (\text{S13})$$

Then equation (S8) becomes

$$\frac{\partial P_+}{\partial z} = \left(\frac{-f_{+0}}{v_+} + \frac{f_{0+} f_{+0}}{v_+ (f_{0+} + f_{0-})} + \frac{f_{0+} f_{-0}}{v_- (f_{0+} + f_{0-})} \right) P_+. \quad (\text{S14})$$

If the factor in parentheses on the right side of this equation is negative, then the length distribution is a exponential with mean length

$$\langle L \rangle = \left(\frac{f_{+0}}{v_+} - \frac{f_{0+} f_{+0}}{v_+ (f_{0+} + f_{0-})} - \frac{f_{0+} f_{-0}}{v_- (f_{0+} + f_{0-})} \right)^{-1}. \quad (\text{S15})$$

We consider the case in which transitions from pausing to growing do not occur, so that $f_{0+} = 0$. Then

$$\langle L \rangle = \frac{v_g}{f_{+0}}. \quad (\text{S16})$$

Note the similarity of this expression to equation (S7) with f_{+0} the effective catastrophe frequency of the model.

2 Experiment

2.1 Cut7-ts strain construction

Cells were cultured using standard fission yeast techniques (62). To construct *cut7-ts* strains with mCherry-tagged tubulin, parent strains with the low-expression *mCherry-atb2* MT marker (39) and the *cut7-24* allele (40) were crossed on malt extract agar plates. Zygotic asci were isolated by digestion with glusulase (PerkinElmer, Waltham, Massachusetts), counted on a haemocytometer, plated onto YE5S agar plates and allowed to grow into colonies. The colonies were replica plated sequentially onto two different plates, first onto YEP (YE5S plus phloxin B) agar plates. Colonies were allowed to grow at 25°C overnight and then placed at 36°C. After 1-2 days, dark pink colonies indicated dead or dying cells and were selected from the parent plates as being positive for *cut7-24*. Next, colonies were replica plated onto YES + 100 µg/mL nourseothricin (Gold Biotechnology, Olivette, Missouri) agar plates. Candidate colonies that grew were selected as positive for *mCherry-atb2*. Candidates with both *cut7-24* and *mCherry-atb2* were validated by imaging fluorescent MTs in monopolar spindles at 36°C using fluorescence microscopy on an Axioplan II light microscope (Carl Zeiss, Jena, Germany) with a 100x, 1.45 NA Plan Fluor oil-immersion objective, a Bioprotechs objective heater (Bioprotechs, Butler, PA) and a Photometrics Cascade 650 CCD camera (Roper Scientific, Sarasota, Florida).

2.2 Measurement of labeled tubulin fraction

A preculture was grown in YPD from which a 50 mL YPD overnight cell culture was grown to late log phase. These cell cultures were pelleted in a tabletop Beckman CS-6 centrifuge, the supernatant was removed, and they were resuspended in 1 mL of NaCl (150 mM)-Tris (50 mM) buffer at pH 8. The cells were washed twice in buffer and resuspended in the same buffer plus 1/2 tablet of complete Mini EDTA-free protease inhibitors (Roche Diagnostics, Mannheim, Germany). The cells were then lysed with a FastPrep FP120 ribolyser (MP Biomedicals, Santa Ana, CA). Lysing tubes were prepared with 1 cm 0.5 µm glass beads on the bottom. 1 mL of cell suspension per tube was lysed on setting 6 for 20 sec for a total of three runs. In between each run, the cells were placed on ice for 10 min. The tubes were spun in a tabletop centrifuge at 5,000 rpm for 6 min and then at 14,000 rpm for 30 min. The clarified lysate was removed and flash frozen with liquid nitrogen.

The cell lysate was mixed 1:1 with Laemmli sample buffer (Bio-Rad, Hercules, CA) plus 5% β-mercaptoethanol. 20 µL samples for ten different lanes were prepared with serial dilutions ranging from 100%-10% of the original cell suspension concentration, and the samples were boiled in water for 7 min. The samples were run on Any KD pre-cast gels in a BioRad Miniprotean II system (Bio-Rad, Hercules, CA) with a Tris (25 mM), glycine (192 mM), 0.1% SDS running buffer. The gels were run for 90 min at 100V with ice packs around the gel box.

Immunoblots were then prepared using a modification of standard techniques. Once transfer sandwiches were assembled, samples were transferred to either a nitrocellulose or a PVDF membrane in transfer buffer consisting of Tris (25 mM), glycine (192 mM), 20% methanol, and 0.05% SDS. Blots were run for 1 hr at 80V. The membranes were transferred to a 5% nonfat milk blocking solution in 1x TBS-T (Tris Buffered Saline plus 0.05% Tween 20) and blocked overnight. The blocked membrane was transferred to a sealable bag containing the primary antibody TAT-1 at a 1:1000 dilution for 1 hr at room temperature. The blots were washed 3 times for 15 min in TBS-T and transferred to a sealable bag containing the secondary antibody Goat-anti-Mouse-AP (Bio-Rad, Hercules, CA) at a 1:1000 dilution for 1 hr at room temperature. The blots were washed 3 times for 15 min in TBS-T and transferred to 20 mL of 1-Step NBI/BCIP developing solution (Thermo Scientific, Waltham, MA) for 30 min.

Strain	Genotype	Source
McI 730	nda3-KM311, cen2::kanr-ura4 ⁺ -lacOp his7 ⁺ ::lacI-GFP,	This study
McI 804	nmt1-GFP-pcp1 ⁺ ::kanr, mcherry-atb2:natMX6, leu1-32, ura4-D18, h ⁻ z:adh15:mcherry-atb2:natMX6, cut7-24, leu1-32, ura4-d18, h ⁹⁰	This study
Original Strains		
McI 728	z:adh15:mcherry-atb2:natMX6, leu1-32, ura4-d18, h ⁺	Y. Wantanabe
McI 789	cut7-24, leu1-32, ura4-d18, h ⁺	I. Hagan

Table S1: Fission yeast strains used in this study.

2.3 Cell preparation for imaging

We grew cells in liquid Edinburgh Minimal Medium (EMM) plus supplements in an overnight preculture, then diluted them over the next 24 hours to keep the cells in mid-exponential growth. Cells were centrifuged at 2,000 rpm for 5 min on a Beckman CS-6 centrifuge (Beckman Coulter, Brea, California). The supernatant was removed and the cells were suspended in 100 μ L of EMM filtered with a 0.2 μ m filter to reduce background fluorescence from the medium. The solution was placed onto 35 mm no. 1.5 glass bottom dishes (MatTek, Ashland, Massachusetts) coated with 8 μ L of 2 mg/mL lectins from *Bandeiraea simplicifolia* (Sigma-Aldrich, St. Louis, Missouri). The cells were allowed to settle and adhere to the lectins for 10 min, then the remaining loose cells were washed away twice with fresh, filtered EMM. 3 mL of fresh, filtered EMM was added to each dish, and the dishes were placed at 36°C.

3 Results

3.1 Sensitivity analysis

We performed sensitivity analysis to check how the capture time and MT mean length vary with model parameters. As discussed in the main text and above, dynamic instability with no boundary effects gives a mean length of $\langle L \rangle = v_g/f_{+0}$ in the slow model and $\langle L \rangle = v_g v_s / (v_s f_c - v_g f_r) \approx v_g/f_c$ in the fast model. To test these relationships, we performed a global sensitivity analysis of the mean capture time and MT length to the dynamic instability parameters. To quantify this sensitivity, we relied on the analysis of the variance of $\langle \tau_c \rangle$ and $\langle L \rangle$ based on the so-called Sobol' decomposition (57), which we computed directly using the PC expansion (58). The dynamic instability parameters were treated as random variables uniformly distributed over the ranges in table 1. The errors from the PC expansion were typically a few percent (ranging from 1-5% depending on which variable and model were fit, table S2). This indicates that the PC expansion is accurately capturing the full simulation results.

The overall contribution of each parameter to the solution variance was quantified using its total Sobol' index (58); a larger value indicates a higher degree of sensitivity of the model to that parameter (table S3). As expected, $\langle \tau_c \rangle$ and $\langle L \rangle$ are most sensitive to the growth speed and effective catastrophe frequency, and this dependence is not altered significantly by the addition of rotational diffusion to the model.

We also determined the local sensitivity of the capture time to these parameters by computing the gradient (the local direction of steepest change) of $\langle \tau_c \rangle$ as a function of the growth speed and catastrophe frequency from the PC expansion, with other parameters fixed at their reference values (fig. S3 shows results for the models without MT rotational diffusion; here the white line follows the local gradient and passes through the reference parameters). This local sensitivity analysis

Slow model	Error
$\langle \tau_c \rangle$ for search and capture	4.9%
$\langle \tau_c \rangle$ with rotational diffusion	3.5%
$\langle L \rangle$ for search and capture	4.4%
$\langle L \rangle$ with rotational diffusion	0.7%
<hr/>	
Fast model	
$\langle \tau_c \rangle$ for search and capture	4.6%
$\langle \tau_c \rangle$ with rotational diffusion	3.5%
$\langle L \rangle$ for search and capture	4.4%
$\langle L \rangle$ with rotational diffusion	1.1%

Table S2: Error in PC expansion.

illustrates the same result found for the global analysis: the capture time is primarily controlled by the growth speed (primarily horizontal arrows in fig. S3) with the main secondary effect from the catastrophe frequency (vertical component of arrows in fig. S3). It also illustrates that the shortest capture times occur for high growth speed and low catastrophe frequency where MT mean lengths are longest.

Total Sobol' indices for slow model	v_g	f_{+0}	v_s	f_{0-}	f_{-0}
$\langle \tau_c \rangle$ for search and capture	0.74	0.32	1.9×10^{-2}	1.8×10^{-2}	8.9×10^{-3}
$\langle \tau_c \rangle$ with rotational diffusion	0.70	0.39	9.2×10^{-3}	1.3×10^{-2}	8.0×10^{-3}
$\langle L \rangle$ for search and capture	0.60	0.42	4.3×10^{-3}	6.5×10^{-3}	3.7×10^{-3}
$\langle L \rangle$ with rotational diffusion	0.52	0.50	4.0×10^{-4}	2.0×10^{-4}	2.0×10^{-4}
<hr/>					
Total Sobol' indices for fast model	v_g	f_c	v_s	f_r	
$\langle \tau_c \rangle$ for search and capture	0.85	0.28	4.0×10^{-3}	7.5×10^{-3}	
$\langle \tau_c \rangle$ with rotational diffusion	0.84	0.28	7.3×10^{-3}	9.9×10^{-3}	
$\langle L \rangle$ for search and capture	0.49	0.39	8.1×10^{-2}	9.5×10^{-2}	
$\langle L \rangle$ with rotational diffusion	0.50	0.39	7.6×10^{-2}	9.7×10^{-2}	

Table S3: Total Sobol' indices.

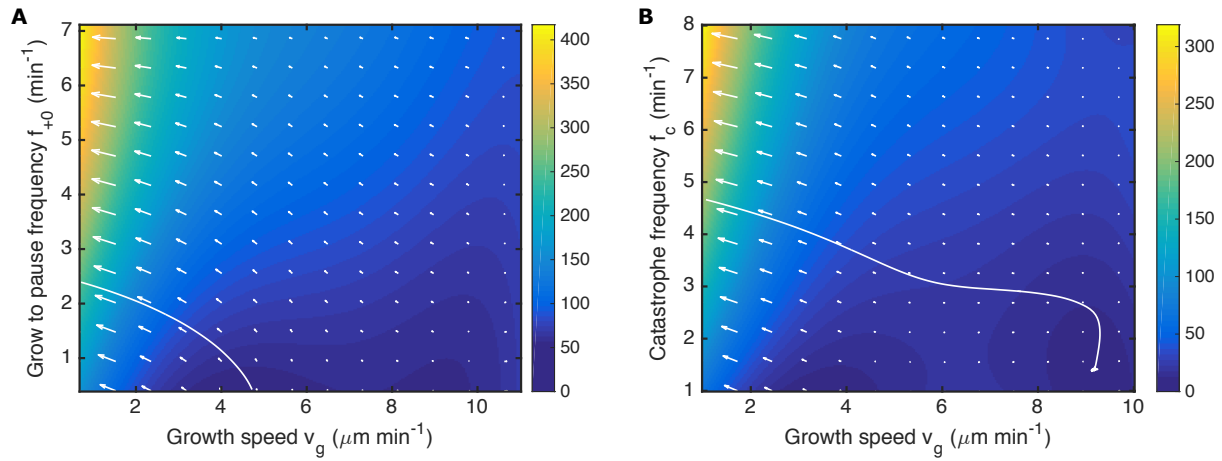


Figure S3: Dependence of capture time on growth speed and effective catastrophe frequency for search and capture model determined from polynomial chaos expansion. (A) Slow model with no MT rotational diffusion. (B) Fast model with no MT rotational diffusion. Color shows capture time in minutes. White arrows show the magnitude and direction of most rapid change in $\langle\tau_c\rangle$ (the gradient). The white line is the curve that follows the gradient and passes through the reference parameter set.

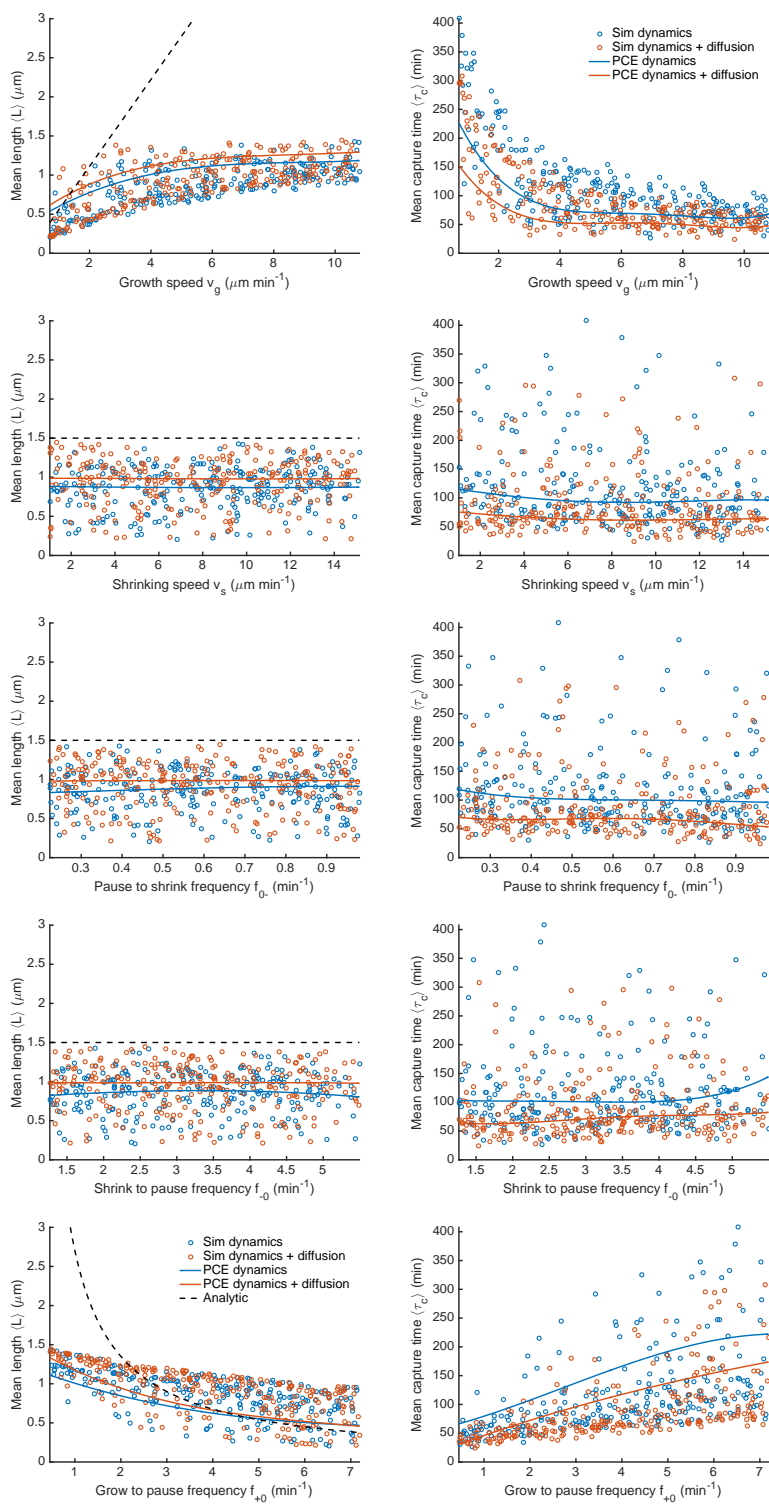
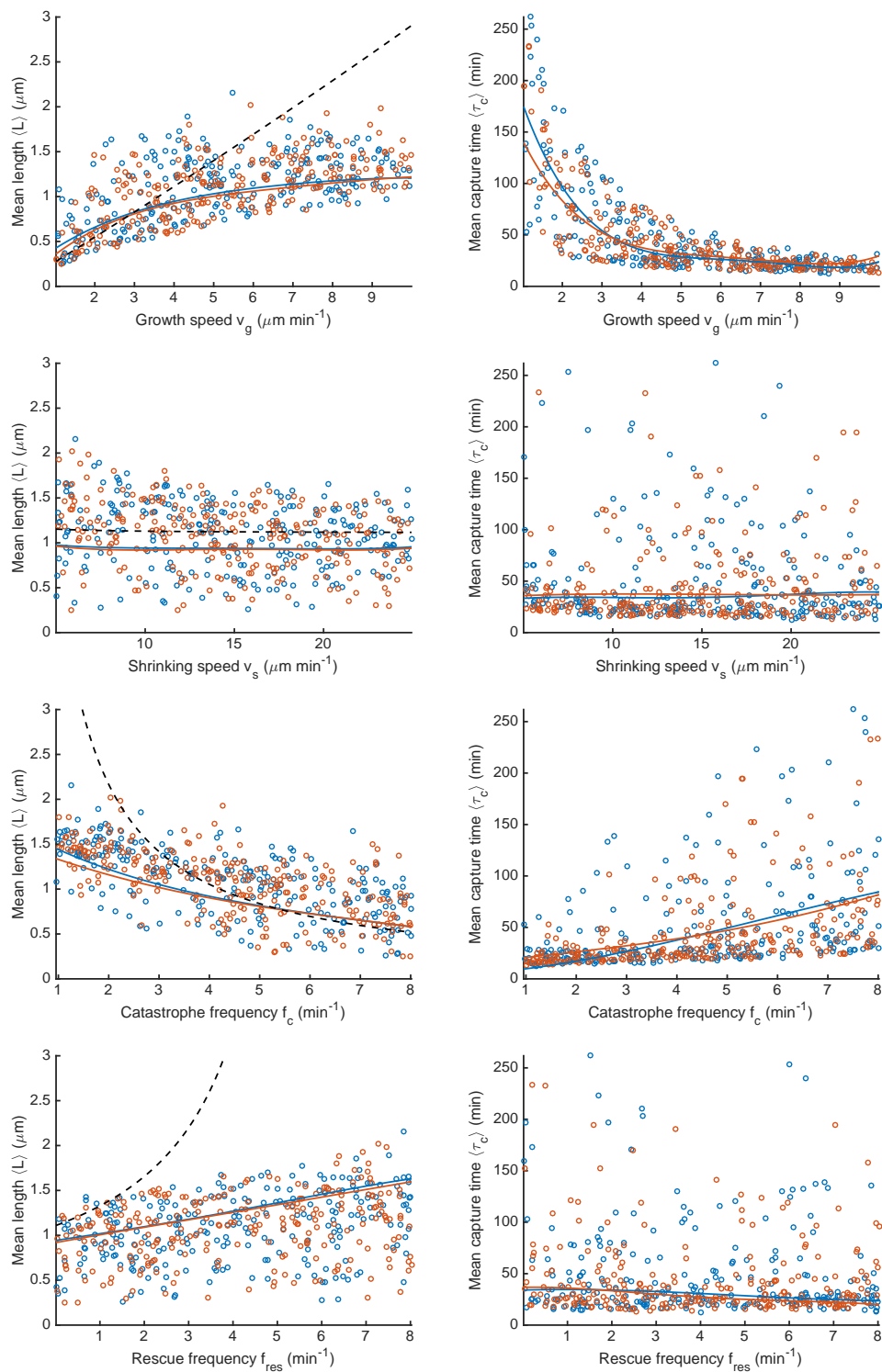


Figure S4: $\langle L \rangle$ and $\langle \tau_c \rangle$ vs. parameters for slow model.

Figure S5: $\langle L \rangle$ and $\langle \tau_c \rangle$ vs. parameters for fast model.